Theory of soliton self-frequency shift in silica optical microresonators with a modified Raman response by the Boson peak

MALONG HU,[1] SHUYI XU,[1] SHULIN DING,[1,4] BING HE,[2] (iD) MIN XIAO,[1] (iD) AND XIAOSHUN JIANG[1,3]

[1]*National Laboratory of Solid State Microstructures, College of Engineering and Applied Sciences, and School of Physics, Nanjing University, Nanjing 210093, China*
[2]*Center for Quantum Optics and Quantum Information, Universidad Mayor, Campus Huechuraba, RM, Chile*
[3]*jxs@nju.edu.cn*
[4]*dingsl@nju.edu.cn*

Abstract: We theoretically study the Raman-induced self-frequency shift of dissipative Kerr soliton in silica optical resonators by taking into consideration the Boson peak. We find that the Boson peak will greatly increase the soliton self-frequency shift and contribute even more than the shift induced by the Lorentzian response for certain pulse durations. We also show that the revised Raman shock time is associated with the pulse width even for a relatively long pulse. Moreover, we demonstrate that the background continuous wave decreases the self-frequency shift of the soliton via the interference with the soliton. Our theoretical and simulated results display excellent agreement with the previous experimental values in the silica-based Kerr-soliton microcomb.

1.   Introduction

Nowadays, dissipative Kerr soliton frequency combs [1,2] have attracted great interest in both nonlinear optical physics and applications, such as integrated optical atomic clocks [3], coherent optical communication [4,5], low noise microwave and terahertz wave signal generations [6–8], and spectroscopy [9,10]. Usually, when the Kerr soliton combs are generated in amorphous materials such as silica and silicon nitride, they will experience a self-frequency shift [11–14] due to the interactions between the Raman nonlinearity and the solitons. This Raman soliton self-frequency shift (SSFS) has an impact on the dynamics [15,16], efficiency [12], bandwidth [17], as well as on the quantum diffusion [18] of the generated solitons. On the other hand, such SSFS, which is important for some practical applications, can be utilized in dual-comb technologies [19,20] based on a single microresonator and low-noise microwave generation with a quiet point [21].

Recently, to model the SSFS in Kerr soliton frequency combs [11,12,15], the Raman response of the materials is usually simplified as a Lorentzian profile [22]. However, the real Raman response in amorphous material exhibits complicated dynamics due to the excess density of vibrational states at Terahertz frequencies [23,24].

To accurately model the Raman response of the amorphous material such as silica, the Boson peak (BP) [24–26], which refers to the significant excess of vibrational modes in the THz range, should be considered. The BP is a characteristic feature of many glassy and amorphous materials, and is believed to play a crucial role in understanding the vibrational states of these materials. Although it has been used to model conventional temporal solitons propagating in optical fibers [27], the influence of the BP on the dissipative Kerr solitons has not been investigated thus far.

In this work, we theoretically investigate the SSFS in silica resonators with a more accurate Raman response function [27]. We surprisingly find that the BP will lead to even more SSFS than that induced by the Lorentzian part of the Raman response. We also derive a revised Raman shock time and point out that the Raman shock time is related to the soliton pulse width even for a relatively long pulse duration. Moreover, we demonstrate that the interference between the continuous-wave (cw) background and the soliton will affect the Raman SSFS.

2.   Theoretical analysis

We begin with the solitonary solution of the generalized mean-field Lugiato-Lefever equation (LLE) [28–30] by taking into account the delayed Raman term [14,17]. Such modified equation that is capable of describing the temporal evolution of the envelope of the optical field circulating in a resonator takes the following form in a co-rotating frame:

$$
\frac{\partial A(t,\tau)}{\partial t} = \left(-\frac{\gamma}{2} - i\Delta\omega\right)A(t,\tau) + i\frac{D_2}{2D_1^2}\frac{\partial^2 A(t,\tau)}{\partial\tau^2} + i(1-f_R)g|A(t,\tau)|^2 A(t,\tau)
$$
$$
+ if_R g\left[h_R(\tau)\otimes|A(t,\tau)|^2\right]A(t,\tau) + \sqrt{\kappa}S_{in}
\tag{1}
$$

where $A(t,\tau)$ is the slowly varying envelope oe optical field, t is the slow time (compared to the roundtrip time), and τ is the fast-time. In Eq. (1), $\gamma = \gamma_0 + \kappa$ stands for the total damping rate of the optical mode with γ_0 and κ representing the intrinsic damping and external coupling rates, respectively, and $\Delta\omega = \omega_p - \omega_0$ denotes the pump-cavity detuning with ω_p. and ω_0 being the pump and resonant frequencies, respectively. In our modeling, we only consider the overall group velocity dispersion D_2. (positive for the requirement of the anomalous dispersion in the Kerr-soliton generation) and use D_1 to characterize the free spectral range (FSR) of the modes. Additionally, g defines the coupling coefficient of the Kerr nonlinearity. In the delayed Raman term, f_R and $h_R(\tau)$ correspond to the Raman fraction and response function, while $\otimes$ denotes the convolution and S_{in} gives the amplitude of the input pump field.

Taking into account the cw background light [29] and treating the Raman term as a perturbation [12], the solitonary solution of single soliton for Eq. (1) can be expressed in the following mathematical form:

$$
A(t,\tau) = A_0 e^{i\varphi_0} + B\,\mathrm{sech}\left(\frac{\tau-\tau_0}{\tau_s}\right)e^{i\Omega(\tau-\tau_0)+i\varphi_s},
\tag{2}
$$

where A_0 and φ_0 stand for the amplitude and phase of the background field, B and φ_s give the amplitude and phase of the soliton field, while τ_0 and τ_s represent the temporal position and pulse width of the soliton envelope in τ-coordinate, respectively, and Ω is the center frequency shift of the single soliton spectrum.

To analyze the soliton evolution in the system, we employ the method of moments [31] and calculate the frequency shift of the single soliton state as

$$
\mu_c = \frac{-i}{4\pi E}\int_{\frac{-\pi}{D_1}}^{\frac{\pi}{D_1}}\left(A^*\frac{\partial A}{\partial\tau} - A\frac{\partial A^*}{\partial\tau}\right)d\tau = \frac{\Omega}{D_1}.
\tag{3}
$$

Note that $E = \frac{1}{2\pi}\int_{\frac{-\pi}{D_1}}^{\frac{\pi}{D_1}}|A|^2 d\tau$ is the average energy of the soliton state inside the cavity. By first taking the time derivative of μ_c in Eq. (3), and then assuming the boundary conditions $A\left(\tau = \pm\frac{\pi}{D_1}\right) = A_0 e^{i\varphi_0}$, and finally performing the integral by parts, one will eventually reach the

following dynamical equation of μ_c with the help of Eq. (1):

$$\frac{\partial \mu_c}{\partial t} = -\gamma \mu_c - \frac{f_R g}{2\pi E} \int_{\frac{-\pi}{D_1}}^{\frac{\pi}{D_1}} \frac{\partial |A|^2}{\partial \tau} (h_R \otimes |A|^2) d\tau. \tag{4}$$

Next, under the condition of the dynamical equilibrium by setting $\frac{\partial \mu_c}{\partial t} = 0$, we obtain

$$\mu_c = -\frac{f_R g}{2\pi \gamma E} \int_{\frac{-\pi}{D_1}}^{\frac{\pi}{D_1}} \frac{\partial |A|^2}{\partial \tau} (h_R \otimes |A|^2) d\tau. \tag{5}$$

From Eq. (5), one can compute the SSFS denoted by Ω_{Raman}, as long as the Raman fraction f_R and the response function $h_R(\tau)$ are available.

Following the previous studies [12,14,22] on the soliton pulses (duration > 100 fs) propagating in the cavities, one can simplify the Raman term to the first order

$$h_R \otimes |A|^2 \approx |A|^2 - \tau_R \frac{\partial |A|^2}{\partial \tau} \tag{6}$$

by means of the Taylor series, where τ_R is the Raman shock time taking the form

$$\tau_R = f_R \int_0^\infty h_R(\tau) \tau d\tau. \tag{7}$$

Under the deep-red-detuned pumping we can adopt a simple *sech*-shape envelop of the optical field to compute Ω_{Raman} [29]:

$$A(t, \tau) \approx B \text{sech}\left(\frac{\tau - \tau_0}{\tau_s}\right) e^{i\Omega(\tau - \tau_0) + i\varphi_s}, \tag{8}$$

since $B \gg A_0$.

By plugging Eq. (6) into Eq. (5) and utilizing Eq. (8), we finally arrive at [12]

$$\Omega_{Raman}^{1st} \approx -\frac{8\tau_R D_2}{15\gamma D_1^2 \tau_s^4} \tag{9}$$

after some algebra. It indicates a τ_s^{-4}-dependence with [12]

$$B\tau_s \approx \frac{1}{D_1} \sqrt{\frac{D_2}{g}}. \tag{10}$$

To theoretically estimate the value of Ω_{Raman} in a silica resonator, we will work with two different forms of the Raman response function $h_R(\tau)$. By the first one we model the Raman-gain spectrum of the fused silica with a single Lorentzian profile [22]:

$$h_{R,1}(\tau) = \frac{\tau_1^2 + \tau_2^2}{\tau_1 \tau_2^2} exp(-\tau/\tau_2) \sin(\tau/\tau_1), \tag{11}$$

where $\tau_1 = 12.2$ fs and $\tau_2 = 32$ fs. In this model, the value of the Raman fraction is $f_{R,1} = 0.18$. Substituting Eq. (11) into Eq. (7) yields an invariable value (denoted as $\tau_{R,1}$) of ~1.46 fs [32]. This result somewhat deviates from those of the previous researches— in Ref. [11], the soliton pulse of 250 fs has a Raman shock time 2.4 fs; in Ref. [21], the soliton pulse of 175-230 fs is with a Raman shock time of 2.5 fs; in Ref. [33], the soliton pulse of 170-200 fs was found to have a Raman shock time of 2.7 fs. All these results based on such oversimplified Lorentz

model neglect the commonly observed phenomenon of the BP in silicon material. The obtained invariable Raman response time $\tau_{R,1}$ in this way [the black solid line in Fig. 2(a)] gives

$$\Omega_{Raman,1}^{1st} \approx -\frac{8\tau_{R,1}D_2}{15\gamma D_1^2 \tau_s^4}. \tag{12}$$

Due to the existence of the BP, we here introduce another improved response function [27], which can explain the appearance of the hump at the frequencies ~2.5 THz of the actual Raman-gain spectrum [see Fig. 1(b)].
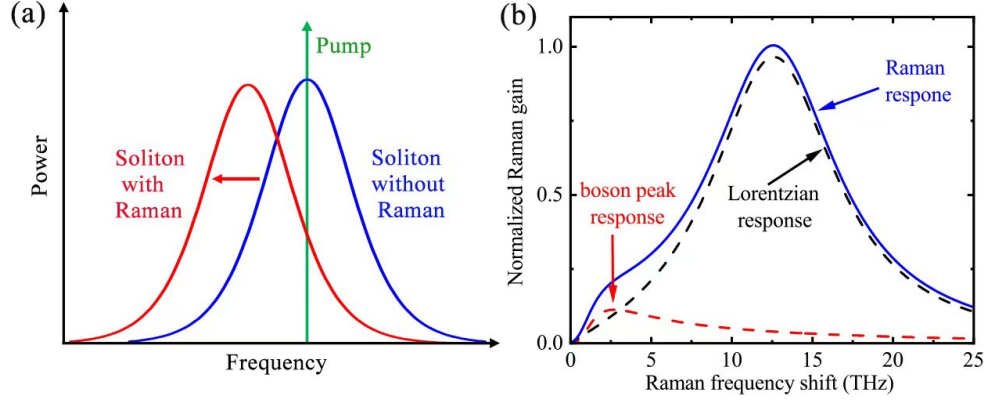

Fig. 1. (a) Illustration for the Raman-induced self-frequency shift of the Kerr-soliton frequency comb. (b) Raman-gain spectrum of the fused silica.

The form of the Raman response thus becomes a linear combination

$$h_{R,2}(\tau) = (1 - f_B)h_{R,1}(\tau) + f_B h_{R,B}(\tau), \tag{13}$$

of the Lorentzian profile and the contribution

$$h_{R,B}(\tau) = \frac{2\tau_b - \tau}{\tau_b^2} exp\left(-\frac{\tau}{\tau_b}\right), \tag{14}$$

from the BP, where $f_B = 0.21$ and $\tau_B = 96$ fs. Here, the response function $h_{R,B}(\tau)$ of the BP is with the Raman fraction $f_{R,2} = 0.245$.

One can simply apply the Raman response function Eq. (13), instead of Eq. (11), to compute τ_R (denoted as $\tau_{R,2}$) with Eq. (7), and it is found to be ~1.57 fs [the blue dash-dotted line in Fig. 2(a)]. After a further examination, however, we find that the result is still far away from the realistic one because the approximation in Eq. (6) has implicitly overlooked the BP response. To clarify this issue, we first notice the integral,

$$\int_0^\infty h_{R,B}(\tau)\tau d\tau = 0, \tag{15}$$

from which one will easily have

$$\tau_{R,2} = f_{R,2} \int_0^\infty h_{R,2}(\tau)\tau d\tau = f_{R,2}(1 - f_B) \int_0^\infty h_{R,1}(\tau)\tau d\tau. \tag{16}$$

Then, under the approximation of the first-order Taylor-series expansion, the contribution of the BP response to the Raman shock time approaches to zero and is thus entirely neglected. To
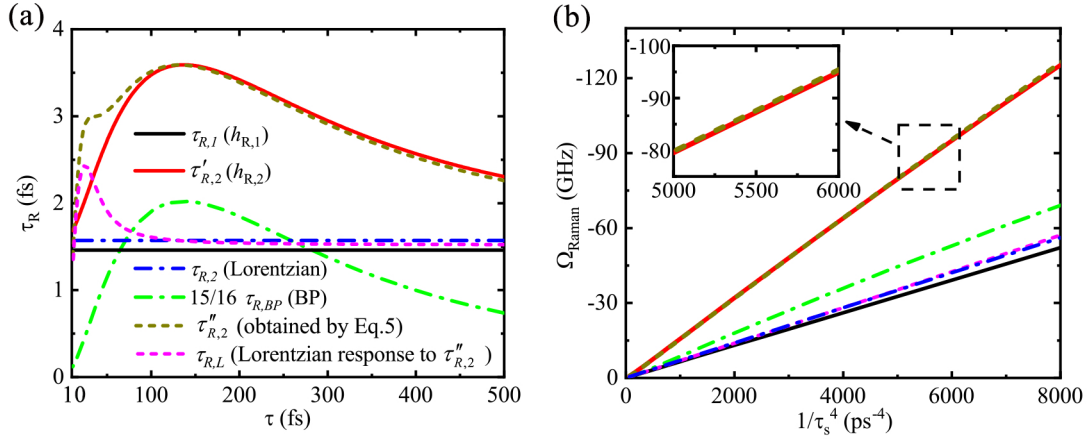
Fig. 2. (a) Raman shock time τ_R as a function of the pulse width τ_s: black solid line, the Raman shock time $\tau_{R,1}$ acquired by Raman response function $h_{R,1}(\tau)$; red solid curve, the corrected Raman shock time $\tau'_{R,2}$ obtained by modified Raman response function $h_{R,2}(\tau)$. The blue and green dash-dotted lines represent the contributions of the Lorentzian response $\tau_{R,2}$ and the BP response $\frac{15}{16}\tau_{R,BP}$ to $\tau'_{R,2}$, respectively. Brown dashed curve, the Raman shock time $\tau''_{R,2}$ directly calculated by Eq. (5) with the function $h_{R,2}(\tau)$. Violet dashed curve, the evaluated contribution of the Lorentzian response $\tau_{R,L}$ to $\tau''_{R,2}$. (b) Corresponding computed values of contributions to the Raman soliton self-frequency shift Ω_{Raman} plotted versus $1/\tau_s^4$, where τ_s ranges from 105 to 300 fs. In the plots, the parameters of the free spectral range, dispersion, and damping rate are set to $D_1 = 2\pi \times 22$ GHz, $D_2 = 2\pi \times 4$ kHz, and $\gamma = 2\pi \times 4$ MHz, respectively.

account for the influence of the BP response to the SSFS, we go back to the precise form of the frequency shift, Eq. (5), while adopting the response function in Eq. (13), and then obtain

$$\Omega_{Raman,2} \approx \Omega^{1st}_{Raman,2} + \Omega_{Raman,BP}. \tag{17}$$

In Eq. (17), the Lorentzian-profile part of the Raman-gain spectrum takes the same form as Eq. (12) but with the factor $\tau_{R,2}$, while the BP contribution

$$\Omega_{Raman,BP} = -\frac{D_1(1-f_B)g}{2\pi\gamma E} \int_{\frac{-\pi}{D_1}}^{\frac{\pi}{D_1}} \frac{\partial |A|^2}{\partial \tau}(h_{R,1} \otimes |A|^2)d\tau \tag{18}$$

can be evaluated with Eqs. (13) and (8). After some algebra, we will obtain

$$\Omega_{Raman,BP} = -\frac{D_2}{2\gamma D_1^2 \tau_s^4}\tau_{R,BP}(\tau_s), \tag{19}$$

where

$$\tau_{R,BP}(\tau_s) = -2f_{R,2}f_B \int_{-\frac{\pi}{D_1}}^{\frac{\pi}{D_1}} \mathrm{sech}^2\left(\frac{\tau}{\tau_s}\right)\tanh\left(\frac{\tau}{\tau_s}\right)\left[h_{R,B}(\tau) \otimes \mathrm{sech}^2\left(\frac{\tau}{\tau_s}\right)\right]d\tau. \tag{20}$$

Putting together the above results involving the BP contribution, we eventually find

$$\Omega_{Raman,2} \approx -\frac{8D_2}{15\gamma D_1^2 \tau_s^4}\tau'_{R,2}, \tag{21}$$

where

$$\tau'_{R,2}(\tau_s) = \tau_{R,2} + \frac{15}{16}\tau_{R,BP}(\tau_s) \tag{22}$$

is the corrected Raman shock time.

Equation (22) shows that the time constant $\tau'_{R,2}$ is related to the pulse width τ_s. In Fig. 2(a), we plot $\tau'_{R,2}$ (red solid curve) as a function of the pulse width, which clearly reveals that the Raman shock time obtained by the complete response function [Eq. (13)] is generally more than twice longer than the time obtained by Eq. (6) for certain pulse durations. In our calculations, we also compute $\tau_{R,2}$ [the contribution of Lorentzian response in linear approximation to $\tau'_{R,2}$, the blue dash-dotted line of Fig. 2(a)] and $\frac{15}{16}\tau_{R,BP}$ (the contribution of BP response, the green dash-dotted line), and find that the contribution of the BP response in $\tau'_{R,2}$ even surpasses that of the Lorentzian response for certain pulse durations. This is due to the fact that as the pulse duration increases, the low-frequency Raman gain gradually contributes more to the Raman shock time. When the pulse duration increases to a certain extent (70-260 fs), the BP response [resonance at ~2.5 THz in Raman spectral, see Fig. 1(b)] dominates in the low-frequency domain. Meanwhile, when the pulse continues to increase (greater than 260 fs), the Lorentzian response contribution in the lower frequency domain (less than 1 THz) dominates again. On the other hand, when the pulse duration is especially short (less than 100 fs), we need to reexamine the contribution of Lorentzian response (denoted as $\tau_{R,L}$ as the violet dashed curve) to Raman shock time through Eq. (5), due to the invalidation of the approximation in Eq. (6). From the calculation [the violet dashed curve in Fig. 2(a)], one may find that the Lorentzian response will dominate when the pulse duration is less than 70 fs. Intriguingly, we notice that $\tau_{R,L}$ will reach a maximum around 23 fs, which can be attributed to the resonant frequency ~12.5 THz of Lorentzian response. In addition, the brown dashed curve in Fig. 2(a) shows the Raman shock time $\tau''_{R,2}$ directly computed from Eq. (5), which indicates that Eq. (22) [the red solid curve in Fig. 2(a)] is a well approach to the Raman shock time given by modified Raman response function when the pulse duration $\tau_s > 100$ fs.

To gain an intuitive comparison of the amount of the Raman SSFS with (the red solid curve) and without (the black one) a consideration of the BP response, we examine Eqs. (12) and (21) using the different pulse widths and respectively plot the corresponding results in Fig. 2(b). As one can see, the SSFS in the presence of the BP is significantly larger than the one in the absence of the BP. The contribution from the BP response (the green dash-dotted line) to the SSFS is also drawn in Fig. 2(b) and, intriguingly, one can see that this contribution is generally larger than that of the Lorentzian response (the blue dash-dotted line) to the SSFS. In Fig. 2, we further compare the analytical values with the numerical ones (the brown dashed curve) by performing the integral of Eq. (5) with the use of Eq. (13). Despite a little discrepancy, we can conclude that Eq. (21) gives a good approximation for the Raman SSFS taking into account the generalized response function in Eq. (13).

3. Numerical simulations

To show the exact SSFS under the effect of BP response, we perform the numerical simulations based on Eqs. (1) and (13) and with the parameters of real silica microresonators. For this purpose we introduce the mode-coupled equations [29] to simulate Eq. (1) and further employ the fast-Fourier-transform method [34] to efficiently deal with the Kerr term. Meanwhile, we process the Raman term as $if_R g F^{-1}\{F[h_R(\tau)] \times F[A(t,\tau)^2]\}A(t,\tau)$, where the symbols $F[\dots]$ and $F^{-1}[\dots]$ represent the Fourier transform and inverse Fourier transform, respectively. In the numerical simulations, we set the wavelength of the pump laser to be 1550 nm and the intrinsic and external decay rates to be $\gamma_0 = 2\pi \times 2$ MHz and $\kappa = 2\pi \times 2$ MHz, respectively. Then, we take the refractive and Kerr nonlinear indexes of the silica to be $n_0 = 1.45$ and $n_2 = 2.2 \times 10^{-20}$ m^2/W, respectively, as well as setting the FSR to be $D_1 = 2\pi \times 22$ GHz. Here, we consider two different resonators with the group velocity dispersions of $D_{2,1} = 2\pi \times 4$ kHz (resonator #1) and $D_{2,2} = 2\pi \times 17$ kHz (resonator #2), respectively. In addition, the effective volumes of the optical modes are estimated as $V_{eff} \approx 5.65 \times 10^{-4}$ mm^3 from the 3-mm-diameter microdisks, which give

the coupling coefficients of the Kerr nonlinearity at $g = 6.75 \times 10^{15}$ Hz/J [29]. These parameters are obtained based on previous works [11,12]. Finally, to trigger the Kerr solitons, we seed the system with the Gaussian pulses [30].

The soliton spectrum of resonator #1 obtained from numerical simulation is displayed in Fig. 3(a). There, we set the pump-cavity detuning to $\Delta\omega = -2\pi \times 7.5$ MHz, to have the corresponding Raman self-frequency shift ~ -97.81 GHz. In Figs. 3(b) and 3(d), we depict the numerically acquired Raman SSFSs (the red dots) against the fitted pulse width in the two silica resonators. We can find that the SSFSs grow with $1/\tau_s^4$, in good agreement with the tendency given by Eq. (21). In addition, one can see that the SSFSs of resonator #1 are much larger than that of resonator #2. This is due to the smaller group velocity dispersion of resonator #1 than that of resonator #2, resulting in the narrower pulse widths of the solitons generated in resonator #1. Correspondingly, the calculated Raman shock times are ~ 3.1 fs for ~ 120 fs of pulse width [see Fig. 3(c)] will decrease to ~ 2.4 fs for ~ 300 fs pulse width [see Fig. 3(e)], and it is in agreement with the previously measured results [11,21,33]. Furthermore, based on numerical simulations, we can calculate that the BP contributes approximately 1.7 fs and 1.1 fs to the Raman shock time in Fig. 3(c) and Fig. 3(e), respectively. The ratios of the BP's contribution to Raman shock time are consistent with that in Fig. 2.

The analytical predictions in Figs. 3(b) and 3(d) (the black solid lines) do not exactly fit the values of the numerically simulated SSFSs (the red dots). Correspondingly, the analytical Raman shock times [the black curves in Figs. 3(c) and 3(e)] are also deviating from the results obtained by $1/\tau_s^4$ fitting of the simulated SSFSs [the red dots in Figs. 3(c) and 3(e)]. A main reason is that the condition $B \gg A_0$ is not usually well satisfied under the actual parameters so that Eq. (10) becomes invalid. Therefore, we need to improve Eq. (21) to

$$\Omega_{Raman,2} \approx -\frac{16\pi g P_{sol}}{15\gamma D_1 \tau_s^2}\tau'_{R,2} \tag{23}$$

proportional to $P_{sol} = \frac{D_1 B^2}{2\pi}$, the intracavity peak power of the soliton field. To calculate P_{sol}, we first use Eq. (2) to fit the simulated soliton envelopes. However, as shown in Figs. 3(b) and 3(d) the values (the green squares) obtained from Eq. (23) still deviate greatly from the numerical simulations (the red dots). We attribute this discrepancy to ignoring the destructive interference between the background light and the soliton due to the out of phase between them, which will decrease the peak power of the generated soliton and mitigate the stimulated Raman scattering effects [see Fig. 4(a)]. In Fig. 4(b), we display the peak power of the soliton with (the red dots) and without (the black dots) consideration of the interference between the soliton and the background light, respectively. And it shows that the interference reduces the peak power of the solitons compared to the case without such interference, even though the intracavity power of the background field ($P_0 = \frac{D_1 A_0^2}{2\pi}$) is much lower than the soliton peak power. Keeping this picture in mind, we recalculate the SSFSs by substituting Eq. (2) into Eq. (5). From Figs. 3(b) and 3(d), one can see that the theoretical Raman SSFSs (the blue stars) considering the interference between the soliton and the cw background light will greatly decrease, and it agrees well with the simulated values (the red dots). Moreover, the corresponding Raman shock times [the blue stars shown in Figs. 3(c) and 3(e)] also match well with numerical values (the red dots). For a comparison, we also plot the analytical values [given by Eq. (12) as the black dashed line in Figs. 3(b) and 3(d)] of the Raman SSFSs without considering the BP and cw background light. According to Figs. 3(b) and 3(d), our theoretical values respectively exceed the analytical ones by 110% for a soliton with the pulse width of approximately 120 fs and by 64% for another soliton with its pulse width of 300 fs.

To better understand the significance and importance of our work, we here provide an example to compare our simulations with the previous experimental results [11]. According to Ref. [11], the Raman shock time and Raman SSFS of a soliton pulse with a pulse width of 150 fs are ~ 2.4
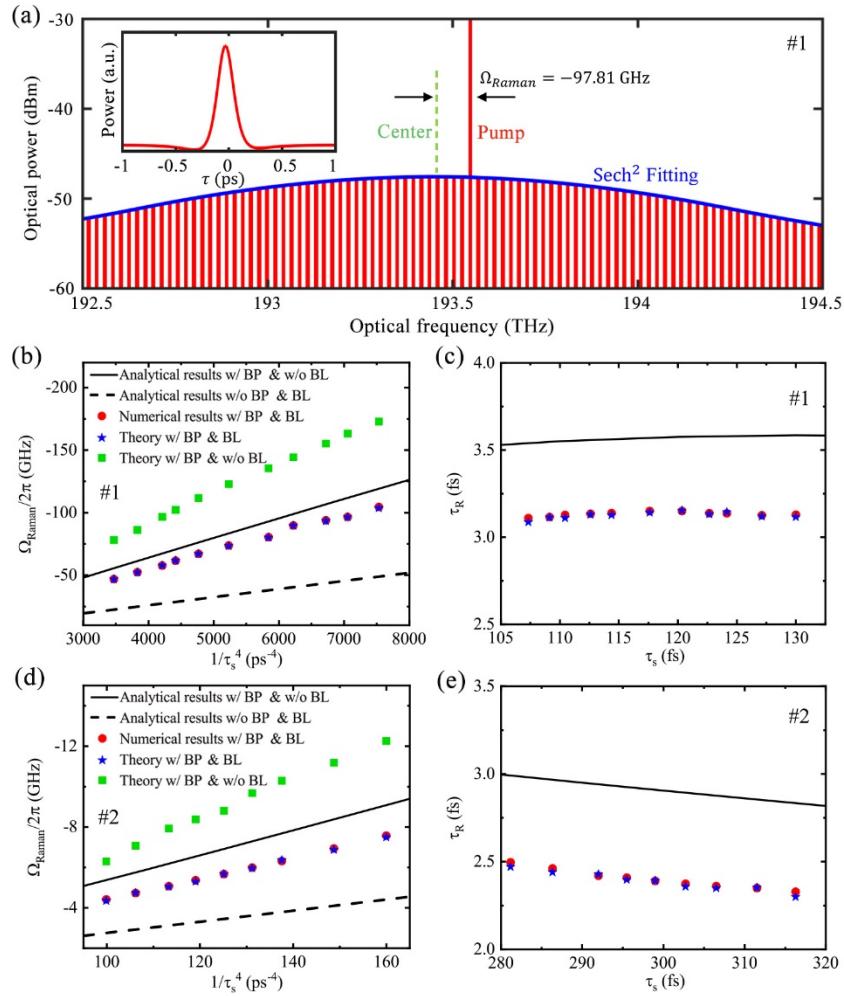
Fig. 3. (a) The soliton spectrum obtained from numerical simulation in resonator 1#, and the insert is the corresponding temporal waveform. (b) and (d), soliton self-frequency shift Ω_{Raman} plotted versus $1/\tau_s^4$. The black solid and dashed lines are the analytical results of the Raman SSFSs calculated from the model including [Eq. (21)] and not including [Eq. (12)] the BP, respectively. The red dots indicate the numerically simulated results. Moreover, the blue stars are the values with the BP and cw background light (BL) obtained from Eq. (5), while the green squares represent the theoretical values acquired with Eq. (23). (c) and (e), the obtained Raman shock time against the pulse width. The red dots are the values acquired from the simulations (with $1/\tau_s^4$ fitting), and the black curve depicts the analytical values of $\tau'_{R,2}$, in addition to the blue stars as the theoretical results considering background fields. (b) and (c) are the results of resonator #1, and (d) and (e) are about resonator #2. The width of the soliton pulse varies with changes in the pump-cavity detuning $\Delta\omega$ (from -2π×5.2 MHz to -2π×7.5 MHz), and the corresponding pump power (80 mW-130 mW) also changes accordingly.

fs and 0.37 THz in the experiment, respectively. Based on Eqs. (1) and (13) (the numerical calculations are based on the parameters derived from Ref. [11]), we generate a soliton with the pulse width of 150 fs and find its corresponding Raman shock time and Raman SSFS are ~2.8 fs and 0.43 THz, respectively, which match well with the experimental results in Ref. [11].
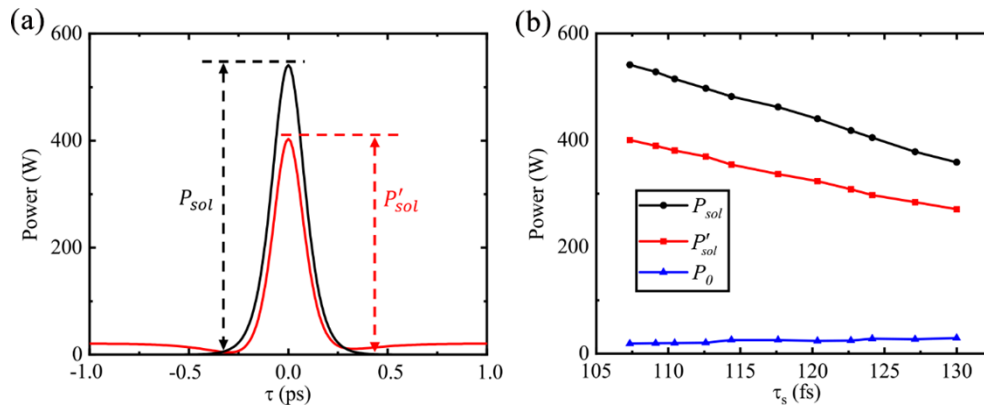
Fig. 4. (a) An example of the soliton temporal profile in resonator #1. The red (black) curve presents the intracavity power of the soliton field with (without) consideration of its interference with the cw background. (b) For different pulse widths τ_s in resonator #1, we fit the intracavity peak powers of the solitons without (P_{sol}) and with (P'_{sol}) considering the interference with the cw background, as well as the powers of corresponding background fields (P_0) inside the resonator.

Furthermore, these simulated results are also consistent with the theoretical ones considering the background field, which are computed with Eq. (5). However, as for the model without including the effect of the BP, its correspondingly simulated Raman shock time and Raman SSFS are respectively ~1.3 fs and 0.20 THz, which considerably deviate from the actual experimental data in Ref. [11]. In addition, we conclude that, in Ref. [11], the BP contributes approximately 1.4 fs and 0.21 THz (58% of the total Raman response) to the Raman shock time and Raman SSFS, respectively, when the soliton has a pulse width of 150 fs. All these results validate the accuracy of our model for the prediction of the Raman SSFS in silica microresonators.

4. Conclusion

In conclusion, we have examined the SSFS of the dissipative Kerr soliton in the presence of the BP in the Raman-gain spectrum of a silica resonator. It is surprisingly found that the contribution from the BP response to the SSFS is non-negligible and even larger than the Lorentzian response part of the Raman effect for certain pulse durations. We also point out that the cw background field will attenuate the peak power of the soliton through an interference, leading to a decrease of the SSFS. One prospect of our study is the modification of the theoretical limitations on the span or efficiency of the dissipative Kerr soliton combs. Although our model is based on silica resonators, the theory is expected to be relevant to other amorphous material platforms such as high-index doped silica [35] or Tantalum oxide [36,37].

Disclosures. The authors declare no conflicts of interest.

Data availability. Data underlying the results presented in this paper are not publicly available at this time but may be obtained from the authors upon reasonable request.

References

1. S. A. Diddams, K. Vahala, and T. Udem, "Optical frequency combs: Coherently uniting the electromagnetic spectrum," Science **369**(6501), eaay3676 (2020).
2. T. J. Kippenberg, A. L. Gaeta, M. Lipson, *et al.*, "Dissipative Kerr solitons in optical microresonators," Science **361**(6402), eaan8083 (2018).

3. Z. L. Newman, V. Maurice, T. Drake, *et al.*, "Architecture for the photonic integration of an optical atomic clock," Optica **6**(5), 680–685 (2019).
4. P. Marin-Palomo, J. N. Kemal, M. Karpov, *et al.*, "Microresonator-based solitons for massively parallel coherent optical communications," Nature **546**(7657), 274–279 (2017).
5. Y. Geng, H. Zhou, X. Han, *et al.*, "Coherent optical communications using coherence-cloned Kerr soliton microcombs," Nat. Commun. **13**(1), 1070 (2022).
6. J. Liu, E. Lucas, A. S. Raja, *et al.*, "Photonic microwave generation in the X- and K-band using integrated soliton microcombs," Nat. Photonics **14**(8), 486–491 (2020).
7. T. Tetsumoto, T. Nagatsuma, M. E. Fermann, *et al.*, "Optically referenced 300 GHz millimetre-wave oscillator," Nat. Photonics **15**(7), 516–522 (2021).
8. D. Kwon, D. Jeong, I. Jeon, *et al.*, "Ultrastable microwave and soliton-pulse generation from fibre-photonic-stabilized microcombs," Nat. Commun. **13**(1), 381 (2022).
9. M.-G. Suh, Q.-F. Yang, K. Y. Yang, *et al.*, "Microresonator soliton dual-comb spectroscopy," Science **354**(6312), 600–603 (2016).
10. A. Dutt, C. Joshi, X. Ji, *et al.*, "On-chip dual-comb source for spectroscopy," Sci. Adv. **4**(3), e1701858 (2018).
11. X. Yi, Q.-F. Yang, K. Y. Yang, *et al.*, "Soliton frequency comb at microwave rates in a high-Q silica microresonator," Optica **2**(12), 1078–1085 (2015).
12. X. Yi, Q.-F. Yang, K. Y. Yang, *et al.*, "Theory and measurement of the soliton self-frequency shift and efficiency in optical microcavities," Opt. Lett. **41**(15), 3419–3422 (2016).
13. C. Bao, Y. Xuan, C. Wang, *et al.*, "Soliton repetition rate in a silicon-nitride microresonator," Opt. Lett. **42**(4), 759–762 (2017).
14. M. Karpov, H. Guo, A. Kordts, *et al.*, "Raman self-frequency shift of dissipative Kerr solitons in an optical microresonator," Phys. Rev. Lett. **116**(10), 103902 (2016).
15. C. Milián, A. V. Gorbach, M. Taki, *et al.*, "Solitons and frequency combs in silica microring resonators: Interplay of the Raman and higher-order dispersion effects," Phys. Rev. A **92**(3), 033851 (2015).
16. Q.-F. Yang, X. Yi, K. Y. Yang, *et al.*, "Counter-propagating solitons in microresonators," Nat. Photonics **11**(9), 560–564 (2017).
17. Y. Wang, M. Anderson, S. Coen, *et al.*, "Stimulated Raman scattering imposes fundamental limits to the duration and bandwidth of temporal cavity solitons," Phys. Rev. Lett. **120**(5), 053902 (2018).
18. C. Bao, M.-G. Suh, B. Shen, *et al.*, "Quantum diffusion of microcavity solitons," Nat. Phys. **17**(4), 462–466 (2021).
19. Q.-F. Yang, B. Shen, H. Wang, *et al.*, "Vernier spectrometer using counterpropagating soliton microcombs," Science **363**(6430), 965–968 (2019).
20. M.-G. Suh and K. J. Vahala, "Soliton microcomb range measurement," Science **359**(6378), 884–887 (2018).
21. X. Yi, Q.-F. Yang, X. Zhang, *et al.*, "Single-mode dispersive waves and soliton microcomb dynamics," Nat. Commun. **8**(1), 14869 (2017).
22. K. J. Blow and D. Wood, "Theoretical description of transient stimulated Raman scattering in optical fibers," IEEE J. Quantum Electron. **25**(12), 2665–2673 (1989).
23. N. Tsuneyoshi, "Boson peak and terahertz frequency dynamics of vitreous silica," Rep. Prog. Phys. **65**(8), 1195–1242 (2002).
24. Y.-C. Hu and H. Tanaka, "Origin of the boson peak in amorphous solids," Nat. Phys. **18**(6), 669–677 (2022).
25. F. Leonforte, A. Tanguy, J. Wittmer, *et al.*, "Inhomogeneous elastic response of silica glass," Phys. Rev. Lett. **97**(5), 055501 (2006).
26. M. Baggioli and A. Zaccone, "Universal origin of boson peak vibrational anomalies in ordered crystals and in amorphous materials," Phys. Rev. Lett. **122**(14), 145501 (2019).
27. Q. Lin and G. P. Agrawal, "Raman response function for silica fibers," Opt. Lett. **31**(21), 3086–3088 (2006).
28. L. A. Lugiato and R. Lefever, "Spatial Dissipative sStructures in Passive Optical Systems," Phys. Rev. Lett. **58**(21), 2209–2211 (1987).
29. T. Herr, V. Brasch, J. D. Jost, *et al.*, "Temporal solitons in optical microresonators," Nat. Photonics **8**(2), 145–152 (2014).
30. C. Godey, I. V. Balakireva, A. Coillet, *et al.*, "Stability analysis of the spatiotemporal Lugiato-Lefever model for Kerr optical frequency combs in the anomalous and normal dispersion regimes," Phys. Rev. A **89**(6), 063814 (2014).
31. G. P. Agrawal, *Nonlinear Fiber Optics* (Springer Berlin Heidelberg, 2000).
32. A. V. Gorbach and D. V. Skryabin, "Light trapping in gravity-like potentials and expansion of supercontinuum spectra in photonic-crystal fibres," Nat. Photonics **1**(11), 653–657 (2007).
33. Q.-F. Yang, Q.-X. Ji, L. Wu, *et al.*, "Dispersive-wave induced noise limits in miniature soliton microwave sources," Nat. Commun. **12**(1), 1442 (2021).
34. T. Hansson, D. Modotto, and S. Wabnitz, "On the numerical simulation of Kerr frequency combs using coupled mode equations," Opt. Commun. **312**, 134–136 (2014).
35. Z. Lu, W. Wang, W. Zhang, *et al.*, "Raman self-frequency-shift of soliton crystal in a high index doped silica micro-ring resonator [Invited]," Opt. Mater. Express **8**(9), 2662–2669 (2018).
36. X. Guo, Z. Degnan, J. A. Steele, *et al.*, "Near-field localization of the boson peak on tantalum films for superconducting quantum devices," J. Phys. Chem. Lett. **14**(20), 4892–4900 (2023).
37. H. Jung, S.-P. Yu, D. R. Carlson, *et al.*, "Tantala Kerr nonlinear integrated photonics," Optica **8**(6), 811–817 (2021).